

Learning a Restricted Boltzmann Machine using biased Monte Carlo sampling

Nicolas Béréux^{1*}, Aurélien Decelle^{1,2}, Cyril Furtlehner² and Beatriz Seoane¹

¹ Departamento de Física Teórica, Universidad Complutense de Madrid, 28040 Madrid, Spain.

² Université Paris-Saclay, CNRS, INRIA Tau team, LISN, 91190, Gif-sur-Yvette, France.

* nicolas.bereux@gmail.com

Abstract

Restricted Boltzmann Machines are simple and powerful generative models capable of encoding any complex dataset. Despite all their advantages, in practice, trainings are often unstable, and it is hard to assess their quality because dynamics are hampered by extremely slow time-dependencies. This situation becomes critical when dealing with low-dimensional clustered datasets, where the time needed to sample ergodically the trained models becomes computationally prohibitive. In this work, we show that this divergence of Monte Carlo mixing times is related to a phase coexistence phenomenon, similar to that encountered in Physics in the vicinity of a first order phase transition. We show that sampling the equilibrium distribution via Markov Chain Monte Carlo can be dramatically accelerated using biased sampling techniques, in particular, the Tethered Monte Carlo method (TMC). This sampling technique solves efficiently the problem of evaluating the quality of a given trained model and the generation of new samples in reasonable times. In addition, we show that this sampling technique can be exploited to improve the computation of the log-likelihood gradient during the training too, which produces dramatic improvements when training RBMs with artificial clustered datasets. When dealing with real low-dimensional datasets, this new training procedure fits RBM models with significantly faster relaxational dynamics than those obtained with standard PCD recipes. We also show that TMC sampling can be used to recover free-energy profile of the RBM, which turns out to be extremely useful to compute the probability distribution of a given model and to improve the generation of new decorrelated samples on slow PCD trained models.

1 Introduction

In Physics, the Restricted Boltzmann Machines (RBM) are *only* a spin system, or an Ising model, for which the coupling matrix between the spins has a bipartite topology. For Machine Learning, it is a famous generative model that has been introduced by Smolensky [1] many decades ago, as one of the first generative models able to learn complex/real datasets with success, and later popularized by Hinton [2, 3], who proposed a practicable algorithm (at that time) to handle the training of these machines. After a short period of fame in which the RBMs were used as a pre-training procedure for bigger neural networks [4, 5], they fell into disuse after 2010, with the introduction of new generative models such as Generative Adversarial Network (GAN) [6] and Variational Autoencoder (VAE) [7]. Indeed, these models have a clear advantage: despite eventual instabilities of the training process, it does not rely on complex and costly Monte Carlo simulations. Yet, RBMs have made a strong comeback in the field of Computational Biology in the last few years mostly for pattern extraction purposes [8–14].

RBMs remain an interesting generative model for many reasons. On the ML part, RBMs are simpler models than GAN or VAE, they only have one hidden layer, thus leading to simple and potentially interpretable learned features. Also, they can learn complex datasets, and are practical

even when the number of samples of this dataset is limited. During the last decade, they have also regained the interest of Physicists [8, 15–18], given their vicinity with the well-known Ising model, for which, in its many variations, the computation of the phase diagram has been a long-standing hobby in the Statistical Physics community. In the case of RBMs, a relevant phase diagram is harder to obtain because the coupling constants of the trained model are necessary correlated because of the learning process. Still, the phase diagram can be used, at least, as a guideline for the model’s parameters and some recent works are trying to analyze the learning dynamics of the models [19].

Despite all these efforts, the training of RBMs remains a difficult task, particularly because of the instability of the training procedure, which is mainly linked to the use of non convergent Markov Chain Monte Carlo (MCMC) processes to estimate the gradient during the training, as identified in a recent work [20]. In this work, we introduce a new learning method using biased sampling Monte Carlo methods [21]. We will show that in some datasets, the classical alternative sampling MCMC method combined with Glauber Heat-Bath dynamics used in the training of the RBMs is impractical: the mixing time of the chain is just too long. Using biased MC sampling, we can avoid this situation, particularly at the beginning of the learning.

This paper is organized as follows. We begin with a definition of RBMs and their classical training procedures in Section 2. We then motivate our work discussing the break of ergodicity phenomena encountered in RBMs trained with data following multimodal distributions in Section 3. After that, we introduce the Tethered MCMC (TMC) sampling method in Section 4, and its combination with the stochastic gradient ascent during the learning process in Section 4.3. In Section 6, we compare the new TMC training strategy with the standard training scheme in several artificial and real datasets.

2 Definitions

An RBM is an Ising spin model with pairwise interactions defined on a bipartite graph of two non-interacting layers of variables: the visible nodes, $\mathbf{v} = \{v_i, i = 1, \dots, N_v\}$, represent the data, while the hidden ones, $\mathbf{h} = \{h_a, a = 1, \dots, N_h\}$, are the latent representations of this data and seek to build arbitrary dependencies between the visible units. Usually, the nodes are binary-valued in $\{0, 1\}$, yet Gaussian or more arbitrary distributions on real-valued bounded support are also used, ultimately making RBMs adaptable for more heterogeneous datasets. Here, we only deal with binary $\{0, 1\}$ variables for both the visible and hidden nodes. Other approaches using truncated-Gaussian hidden units [22], giving a ReLu type of activation functions for the hidden layer do work well, but our experiments shouldn’t be affected by this choice. The energy function of an RBM is taken as

$$E[\mathbf{v}, \mathbf{h}; \mathbf{w}, \mathbf{b}, \mathbf{c}] = - \sum_{ia} v_i w_{ia} h_a - \sum_i b_i v_i - \sum_a c_a h_a, \quad (1)$$

with \mathbf{w} being the weight matrix, and \mathbf{b}, \mathbf{c} the visible, and hidden biases (or the magnetic fields in the Physics language), respectively. The Boltzmann distribution of such a model is then given by

$$p[\mathbf{v}, \mathbf{h} | \mathbf{w}, \mathbf{b}, \mathbf{c}] = \frac{\exp(-E[\mathbf{v}, \mathbf{h}; \mathbf{w}, \mathbf{b}, \mathbf{c}])}{Z}, \quad (2)$$

where Z is the partition function. RBMs are usually trained using gradient ascent of the log-likelihood function, \mathcal{L} , of the training dataset, $\mathcal{D} = \{\mathbf{v}^{(1)}, \dots, \mathbf{v}^{(M)}\}$, being \mathcal{L} defined as

$$\begin{aligned}\mathcal{L}(\mathbf{w}, \mathbf{b}, \mathbf{c} | \mathcal{D}) &= M^{-1} \sum_{m=1}^M \ln p(\mathbf{v} = \mathbf{v}^{(m)} | \mathbf{w}, \mathbf{b}, \mathbf{c}) \\ &= M^{-1} \sum_{m=1}^M \ln \sum_{\{\mathbf{h}\}} e^{-E[\mathbf{v}^{(m)}, \mathbf{h}; \mathbf{w}, \mathbf{b}, \mathbf{c}]} - \ln Z.\end{aligned}$$

The gradient of \mathcal{L} is then composed of two terms: the first one accounts for the interactions between the RBM's response and the training set, and the same for the second, but using the samples drawn by the machine itself. The expression of the \mathcal{L} gradient w.r.t. all the parameters is given by

$$\frac{\partial \mathcal{L}}{\partial w_{ia}} = \langle v_i h_a \rangle_{\mathcal{D}} - \langle v_i h_a \rangle_{\mathcal{H}}, \quad (3)$$

$$\frac{\partial \mathcal{L}}{\partial b_i} = \langle v_i \rangle_{\mathcal{D}} - \langle v_i \rangle_{\mathcal{H}}, \quad (4)$$

$$\frac{\partial \mathcal{L}}{\partial c_a} = \langle h_a \rangle_{\mathcal{D}} - \langle h_a \rangle_{\mathcal{H}}, \quad (5)$$

where

$$\langle f(\mathbf{v}, \mathbf{h}) \rangle_{\mathcal{D}} = M^{-1} \sum_m \sum_{\{\mathbf{h}\}} f(\mathbf{v}^{(m)}, \mathbf{h}) p(\mathbf{h} | \mathbf{v}^{(m)}),$$

denotes an average of an arbitrary function $f(\mathbf{v}, \mathbf{h})$ over the dataset, and $\langle f(\mathbf{v}, \mathbf{h}) \rangle_{\mathcal{H}}$, the average over the Boltzmann measure in Eq. (2).

A large part of the literature on RBMs focuses on schemes to approximate the r.h.s. of Eqs. 3-5, usually called the *negative term* of the gradient. In theory, these terms can be computed up to an arbitrary precision using parallel MCMC simulations, as long as the number of MC steps are large enough to ensure a proper sampling of the equilibrium configuration space. The most popular approximation schemes to compute the negative part are: (i) the Contrastive Divergence (CD), introduced decades ago by Hinton [3], or its later refinement the (ii) Persistent CD (PCD) [23]. In both cases, the negative part of the gradient is estimated after a few k sampling steps, typically $k \sim \mathcal{O}(1)$, and the differences are just related to different clever ways of initializing the Markov chains. In the CD recipe, the parallel MCMC simulations are initialized from the same samples of the mini-batch as the ones used to compute the positive part of the gradient, while in the PCD one, the ending configurations of each Markov chain are saved from one parameter update to the next to initialize the subsequent chain. In practice, the consequences of the lack of convergence of all these MCMC processes under these approximations during the learning has been very rarely studied in the Literature, and it has been recently shown that it produces dramatic and non-monotonous effects in the generating performance of RBMs [20]. In fact, this work showed that the CD method is, in general, a very bad training method because it fits models whose equilibrium distribution differs drastically with the dataset distribution. In contrast, the PCD recipe seemed to fit RBMs with good equilibrium properties in images' datasets, but the quality of the samples generated with those machines was limited by the number of sampling steps k used during the learning.

A more precise investigation of the PCD scheme shows us examples where this strategy completely fails to learn good model parameters too. For instance, it was shown in [24] that simple

artificial datasets of low-effective dimension, such as well-separated clusters of points, cannot be learned correctly with PCD. One would naively think that such a simple dataset should be straightforward to learn with an RBM, considering that this is a problem easily solved with a Gaussian Mixture model. On the contrary, the major problem of such “clustered” datasets, is that sampling ergodically the configuration space of multimodal distributions is very hard. For instance, in a one-dimensional case, that is, clusters separated along one spatial direction, the typical probability density profile along that direction should correspond to well-adjusted Gaussian peaks centered at each cluster center, separated by regions with essentially zero probability. It is known that in such case, the MCMC chains can take an extremely long time to jump from one cluster to another. In Physics we would speak in terms of large free-energy barriers to surmount, and it is exactly the same phenomena one encounters in the surroundings of a first-order phase transition. This tends to demonstrate that a learning procedure relying on parallel MCMC samplings to estimate the correlations of the model, should be extremely costly or even fail miserably when trying to learn *clusterized* data.

Many interesting datasets form compact clusters after dimensional reduction, which is, for instance, the typical case of genome or protein sequence data. The previous discussion anticipates that not only obtaining reliable effective models for such datasets using standard learning schemes (such as CD/PCD) must be hard, but also evaluating the quality of a given trained model. Indeed, standard sampling techniques fail to equilibrate, which means that a convergent generation sampling can be prohibitively long. As a consequence, approximate techniques typically used to compute \mathcal{L} , such as Importance Sampling [25] must be completely inaccurate in such datasets.

The numerical problems accompanying the apparition of multiple coexisting phases have been long-faced in Physics or Chemistry. One of the possible solutions is to break the metastability with external constraints. This idea can be easily implemented using biased-MC or reweighting methods, such as the Umbrella Sampling method [26], microcanonical methods [27, 28], or the Tethered MC (TMC) method [29–31], that will be adapted here to the training and generation sampling of RBMs.

3 Breakdown of ergodicity

Multimodal distributions are notoriously hard to sample because simulations get trapped in one or several metastable free energy minima for a very long time and fail to visit the entire configuration space. We illustrate this difficulty in Fig. 1. With this aim, we have considered an artificial dataset of 5 clusters of points in 1000 dimensions, all 5 aligned in one single dimension, for which it is possible to train exactly an RBM as discussed in Ref. [24]. We use this perfectly trained RBM to generate new data either using standard MCMC moves (using Glauber Heath Bath dynamics),—a sampling procedure that will be denoted as SMC from now on—, or with the TMC method that will be introduced later. In both cases, the term MC sweeps, refers to an attempt to update all the N_v and N_h variables of the model.

Before continuing with the discussion of the Fig. 1, let us briefly discuss the projections we use to compare the original and generated datasets. We begin by extracting the principal components of the dataset ω_α with $\alpha = 0, \dots, N_v - 1$ following the standard Principal Component Analysis (PCA). Thus, ω_0 , marks the direction of maximum variance of the dataset, ω_1 the next one, and so on (with the constraint of being all $\{\omega_\alpha\}$ orthonormal). Now, we use these directions to project

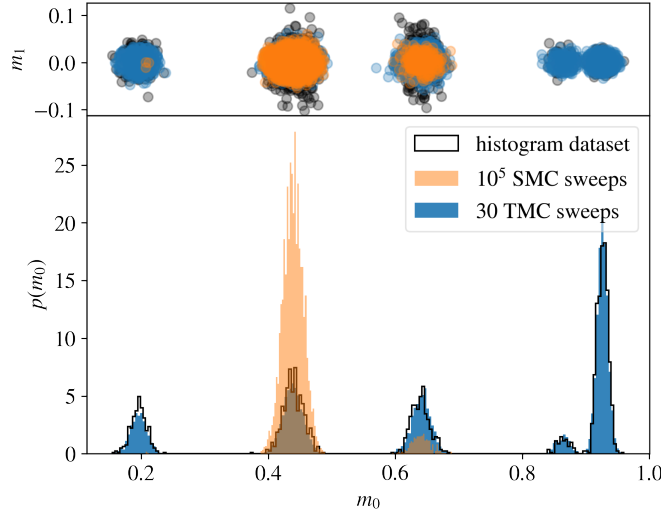


Figure 1: We illustrate the difficulties of sampling a multimodal distribution with standard Glauber MC moves of a dataset of 5 aligned point clusters in high dimensions. On the top, we show the projection of the dataset/generated samples along the first (m_0) and the second (m_1) dataset’s principal components. Each dot is one sample. In the bottom, we show the histogram of all these m_0 . The original dataset is displayed in black, and the generated datasets are shown in blue or orange, depending on the algorithm used to sample the configuration space of the exactly trained RBM from Ref. [24], from random initializations. Orange samples are obtained after 10^5 standard Glauber MC (SMC) steps and blue samples, after 30 TMC sweeps.

each data point, $\mathbf{v}^{(m)}$,

$$m_\alpha^{(m)} = \frac{\mathbf{v}^{(m)} \cdot \boldsymbol{\omega}_\alpha}{\sqrt{N_v}}, \quad (6)$$

which defines the datum’s *magnetization* along the α principal direction. In Fig. 1, we show the first two magnetizations, $m_0^{(m)}$ and $m_1^{(m)}$, and the distribution $p(m_0^{(m)})$ for the different sets of data. Note that one needs just one direction to split up the 5 clusters (they are aligned by construction), and it is straightforward to capture such a direction with the PCA. The choice of using the PCA in general will be justified in Sect. 5. Clearly, from a random initialization, local SMC moves get trapped in just one of the 5 data clusters even after performing 10^5 MC sweeps, thus failing to visit (and generate) data in the rest of the clusters. The breakdown of ergodicity is easy to understand here: in order to jump from one cluster to another with local moves, the trajectory must visit configurations with an intermediary m_0 , and such configurations have extremely low probability. In the TMC sampling, one can enforce the simulations to visit these rare but crucial intermediate states by introducing external constraints. As a result, this sampling method is able to generate samples in all the five clusters with the correct associated weights.

4 Sampling with the tethered MC method

We use the TMC sampling method [29,31] to sample efficiently the configuration space of clustered models. TMC is a refinement over the popular Umbrella Sampling method [26] that permits simplifying notably the reconstruction of canonical expected values. This simplification will be crucial to combine this sampling technique with the stochastic training dynamics. In the TMC method, a soft constraint $m(\mathbf{v}) \sim \hat{m}^1$ is introduced in the partition function Z via the identity

$$\sqrt{\alpha/2\pi} \int_{-\infty}^{\infty} d\hat{m} e^{-\frac{\alpha}{2}(m(\mathbf{v})-\hat{m})^2} = 1,$$

where α controls the strength of the constraint. In this way, Z can be written in terms of the TMC effective potential, $\Omega(\hat{m})$,

$$Z = \int_{-\infty}^{\infty} d\hat{m} e^{-\alpha\Omega(\hat{m})}, \quad (7)$$

with

$$e^{-\alpha\Omega(\hat{m})} = \sqrt{\frac{\alpha}{2\pi}} \sum_{\{\mathbf{h}, \mathbf{v}\}} e^{-E(\mathbf{h}, \mathbf{v}) - \frac{\alpha}{2}[m(\mathbf{v}) - \hat{m}]^2}. \quad (8)$$

Then, the probability of \hat{m} is given by

$$p(\hat{m}) = \frac{e^{-\alpha\Omega(\hat{m})}}{Z}. \quad (9)$$

Clearly, when $\alpha \rightarrow \infty$, $p(\hat{m})$ recovers the canonical probability of finding $m(\mathbf{v}) = \hat{m}$, that is, $\langle \delta(m(\mathbf{v}) - \hat{m}) \rangle$. Finite values of α soften this constraint, which is necessary to facilitate sampling. We can use this probability to define a new ensemble, the *tethered ensemble*, where $m(\mathbf{v}) \sim \hat{m}$. Then, the expected value of an observable $O(\mathbf{h}, \mathbf{v})$ in this ensemble is

$$\langle O \rangle_{\hat{m}} = \frac{\sum_{\{\mathbf{h}, \mathbf{v}\}} O(\mathbf{h}, \mathbf{v}) \omega(\mathbf{h}, \mathbf{v}, \hat{m})}{\sum_{\{\mathbf{h}, \mathbf{v}\}} \omega(\mathbf{h}, \mathbf{v}, \hat{m})}, \quad (10)$$

with

$$\omega(\mathbf{h}, \mathbf{v}, \hat{m}) = e^{-E(\mathbf{h}, \mathbf{v}) - \frac{\alpha}{2}[m(\mathbf{v}) - \hat{m}]^2}. \quad (11)$$

Now, the principal innovation of the TMC method is realizing that

$$\Omega'(\hat{m}) = \frac{d\Omega}{d\hat{m}} = \langle \hat{m} - m(\mathbf{v}) \rangle_{\hat{m}}, \quad (12)$$

which means that $\Omega(\hat{m})$ can be recovered up to any desired precision, from a numerical integration of Monte Carlo averages of several independent simulations at fixed \hat{m}

$$\Omega(\hat{m}) - \Omega(\hat{m}_{\min}) = \int_{\hat{m}_{\min}}^{\hat{m}} \frac{d\Omega}{d\hat{m}'} d\hat{m}' = \int_{\hat{m}_{\min}}^{\hat{m}} \langle \hat{m}' - m(\mathbf{v}) \rangle_{\hat{m}'} d\hat{m}'. \quad (13)$$

So does $p(\hat{m})$,

$$\frac{e^{-\alpha\Omega(\hat{m})}}{\int_{\hat{m}_{\min}}^{\hat{m}_{\max}} e^{-\alpha\Omega(\hat{m}')} d\hat{m}'} \rightarrow p(\hat{m}), \quad (14)$$

¹technically the global constraint could perfectly concern both the visible and the hidden units, $m(\mathbf{h}, \mathbf{v}) \sim \hat{m}$, or only the hidden $m(\mathbf{h}) \sim \hat{m}$ too.

as long as, \hat{m}_{\min} and \hat{m}_{\max} , the two extrema of the integration interval, are safely chosen so that $e^{-\alpha\Omega(\hat{m})}$ is essentially zero beyond that range. Also, $p(\hat{m}) \approx \langle \delta(m(\mathbf{v}) - \hat{m}) \rangle_{\mathcal{H}}$ for large α . In this work, we use typically $\alpha \sim 10^4$, which means that the approximation is rather good. In addition, we can exploit the TMC strategy to estimate the free energy barrier between two metastable states.

Interestingly, it is straightforward to show that the canonical average of O , $\langle O \rangle_{\mathcal{H}}$, that is, the average with respect to the Boltzmann measure of Eq. (2) (the quantity one wants to compute in practice), can be recovered using the following identity:

$$\langle O \rangle_{\mathcal{H}} = \int_{-\infty}^{\infty} \langle O \rangle_{\hat{m}} p(\hat{m}). \quad (15)$$

In other words, model averages can be recovered up to any desired precision just by integrating TMC averages (with no approximation involved). Such a turnover between ensembles is only useful if sampling ergodically the TMC measure (11) is much easier than in the original unconstrained problem (2). This is particularly true when only one phase is stable at a given \hat{m} . In the absence of metastabilities, thermalization is extremely fast. This means that one can use the TMC weight of Eq. (11) to avoid phase coexistence (and long time dependencies) in your MC simulation.

4.1 Example: TMC Sampling of the 5 aligned cluster dataset

Let us come back to the 5 clusters dataset example used to illustrate the ergodicity problem (discussed around Fig. 1). In the light of the preceding discussion, it is now clear that we can efficiently sample the whole configuration space running TMC simulations with \hat{m} running in the range of observed m_0 . We have summarized the TMC sampling procedure for this example in Fig. 2. The first step is to discretize the range of m_0 needed to integrate numerically $\Omega'(\hat{m})$ in (13) and to obtain $p(\hat{m})$ (14). To do this, we need to select a good interval of \hat{m} , that is, a \hat{m}_{\min} and \hat{m}_{\max} . We can do this using the minimum and maximum projection of the dataset along ω_0 , plus a safety border to ensure zero probability beyond these points. In order to avoid scaling problems between RBMs models when defining \hat{m} , we have always normalized the data projections conveniently, so that they lie in the interval $[0, 1]$, and considered extra borders of ± 0.1 or ± 0.2 to define the range of \hat{m} . Then, we discretize uniformly the interval $[\hat{m}_{\min}, \hat{m}_{\max}]$ using $N_{\hat{m}}$ points (for the sampling in Fig. 2 we considered 250 discretization points, even though we show much less in the sketch to enhance the comprehension). Then, we run independent TMC simulations at each of these \hat{m} values. In general, we consider several parallel runs for each \hat{m} to estimate $\Omega'(\hat{m})$ in (12). This is much faster than iterating TMC many times because they can run in parallel. Note that, the TMC weight of Eq. (11) breaks the independence of the visible units provided by the bipartite lattice structure, which means that we lose the possibility of updating all visible variables at the same time (the so-called alternating Gibbs sampling) which makes the TMC simulations much slower than the unconstrained model. Once we have computed $\Omega'(\hat{m})$ for all the discretized values of \hat{m} , we integrate this function numerically to extract Ω and $p(\hat{m})$. We compare the $p(\hat{m})$ extracted following this pipeline² with the histogram of m_0 obtained from the dataset in Fig. 3, showing a perfect match between both distributions. Finally, one can use this $p(\hat{m})$ to improve the estimation of the \mathcal{L} gradients via Eq. (15) during the learning process, as we will discuss below, or just to generate samples from our model. In this second case, the procedure is simple, draw a set of $\hat{m}_{\text{sampling}}$ values from the $p(\hat{m})$ distribution, and run independent and short TMC runs (initialized

²actually $p(\hat{m})$ versus $\langle m_0(\mathbf{v}) \rangle_{\hat{m}}$ for the whole range of \hat{m} simulated

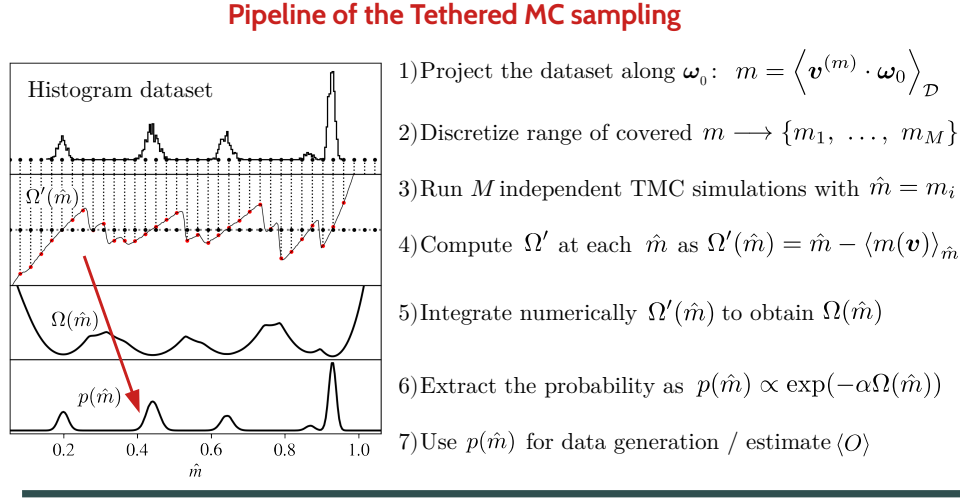


Figure 2: We describe the basic steps of the TMC sampling process that can be used either to generate equilibrium samples of the model, or to estimate the log-likelihood gradient during the training.

at random or other non-informative configuration) at these \hat{m} s. The distribution of the projections of the samples generated using this procedure were shown in blue in Fig. 1, showing again a perfect match with the distribution of the original dataset.

4.2 Generalization to multiple order parameters

The method can easily be generalized to k constraints. Let $\mathbf{m} = (m_1, \dots, m_k)$ represent these parameters. The method remains the same: a constraint is imposed on the parameters at the same time, hence the weights of the TMC ensemble are now given by :

$$\omega(\mathbf{h}, \mathbf{v}, \hat{\mathbf{m}}) = e^{-E(\mathbf{h}, \mathbf{v}) - \frac{\alpha}{2} \sum_{l=1}^k (\hat{m}_l - m_l)^2}. \quad (16)$$

The gradient of the potential is now

$$\nabla \Omega(\hat{\mathbf{m}}) = \langle \hat{\mathbf{m}} - \mathbf{m} \rangle_{\hat{\mathbf{m}}}, \quad (17)$$

and the potential can be recovered at fixed $\hat{\mathbf{m}}$ through the numerical integration of $\nabla \Omega(\hat{\mathbf{m}})$:

$$\Omega(\hat{\mathbf{m}}) = \Omega(\hat{\mathbf{m}}_{\min}) + \int_{\mathcal{C}} \nabla \Omega(\hat{\mathbf{m}}') d\hat{\mathbf{m}}', \quad (18)$$

where \mathcal{C} represents any path leading from $\hat{\mathbf{m}}_{\min} = (\hat{m}_{1,\min}, \dots, \hat{m}_{k,\min})$ to $\hat{\mathbf{m}}$. Finally, $p(\hat{\mathbf{m}})$ can be recovered analogously to the single order parameter case (14).

4.3 Training RBM with the Tethered Monte Carlo method

The TMC method is therefore very efficient to sample quickly isolated clusters. It is then straightforward to use it to compute the negative term of the gradient eqs. (3-5). For this goal, we need to run several independent simulations at fixed \hat{m} and estimate $\langle s_i \rangle_{\hat{m}}$, $\langle \tau_a \rangle_{\hat{m}}$ and $\langle s_i \tau_a \rangle_{\hat{m}}$. We then

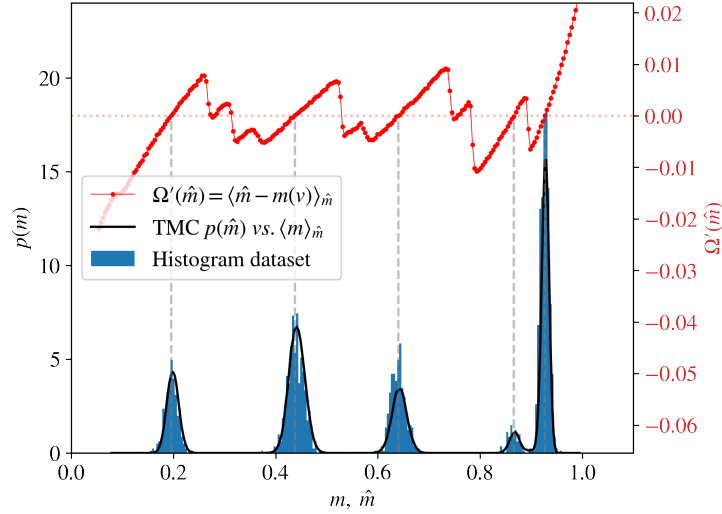


Figure 3: Reconstruction of the data probability distribution profile using the TMC sampling. In red, we show the derivative of the TMC effective potential, $\Omega'(\hat{m})$, obtained from TMC simulations at fixed values of \hat{m} and $\alpha = 2 \cdot 10^4$. In black we show the Tethereed probability $p(\hat{m})$ obtained from the numerical integration of $\Omega(\hat{m})$ plotted versus $\langle m \rangle_{\hat{m}}$. We compare this probability with the histogram of the dataset projection along ω_0 , showing an almost perfect match, even if the two probabilities should coincide only in the limit $\alpha \rightarrow \infty$.

recover the unconstrained negative term of the gradient using a numerical integration as in (15). In order to improve statistics in the gradient computation, we average each observable O , not only using M parallel samples (running each at fixed \hat{m}), but also in time T thermal history. This means that each $\langle O \rangle_{\hat{m}}$ is estimated by

$$\overline{O}^{\hat{m}} = \frac{1}{M} \sum_{k=1}^M \frac{1}{T} \sum_{t=1}^T O^{(k)}(t), \quad (19)$$

during the simulation.

5 Learning dynamics and principal components of the dataset

RBM's have been thoroughly studied during the last decade in the context of statistical physics (see Ref. [18] for a recent review on the topic) and very important progresses have been made related to the understanding of their thermodynamics and learning mechanisms [8, 15, 17, 19]. In particular, we now know that the RBM's pattern encoding process is triggered by learning the PCA of the dataset, i.e. the directions $\{\omega_\alpha\}$ introduced in Sect. 3. At the beginning of the learning, when the machine is in a paramagnetic state [16, 32, 33], the learning dynamics can be easily understood when decomposing the RBM's weight matrix onto its singular value decomposition (SVD), $\mathbf{w} = \mathbf{U}\mathbf{\Sigma}\mathbf{V}^T$, and projecting the gradient equations 3-5 onto each of these modes. In the regime where all the elements of \mathbf{w} are small, it can be shown that the first columns of \mathbf{V} progressively align with the principal components of the dataset one by one, a process that can be

easily followed through the emergence of new eigenvalues in the SVD. At larger learning times, the linear approximation of the gradient is no longer valid and the relation between the dataset's principal directions and the ones of the weight matrix is no longer true.

This means that in the early times of the learning process, the RBM passes from being in a paramagnetic phase to a ferromagnetic phase, with non-zero magnetizations m_α (recall (6)) along a growing number of directions α , related to the number of the dataset's principal components encoded in the SVD rotation matrix V and the number of hidden nodes of the RBM. We also know that the relevant directions to project the data are for some time $\{\omega_\alpha\}$, and therefore related to the eigenmodes of the weight matrix. These theoretical results suggest that m_α must be good order parameters to control thermalisation (and to break metastabilities) at least for some time. The main drawback here, is that the longer the learning, the higher the number of constraints needed to sample ergodically the phase space. In the following, we will use the TMC method to constraint the value of the magnetization along 1 or 2 fixed PCA directions.

6 Results

In this section, we will compare the quality and the dynamics of RBMs trained using either the standard Glauber MC updates (SMC), or our new TMC sampling strategy to estimate the negative part of the \mathcal{L} gradient. In both cases, we will always keep the PCD initialisation scheme to enhance as much as possible the thermalisation during the training and perform the same number of Gibbs steps between each parameter update. We further designate SMC-RBM to machines trained with the usual procedure (SMC), and TMC-RMB, to machines trained with TMC. We begin with results on artificial datasets to end with applications in real ones.

6.1 Artificial datasets

To illustrate the TMC learning strategy, we will first analyze the learning process of artificial datasets. At a second stage, we will move to real clustered datasets. We will consider 2 different high-dimensional datasets having $N_v = 1000$ visible variables both. The first one, consists of two clusters supported on a one-dimensional subspace given by the vector $\mathbf{u} = \mathbf{1}/\sqrt{N_v}$. The second, is made of three separated clusters supported on a two-dimensional subspace. Both datasets were created to exaggerate a clustered nature, this means that, points are generated so they form compact clusters separated by large empty regions. In both cases, points can be easily split up in clusters by projecting the dataset on the first (ω_0 , for the 1D case) or the first 2 (ω_0 and ω_1 for the 2D case) principal components of the dataset.

In this type of datasets, we expect that a simple spin-flip-type MCMC algorithm, fails dramatically to sample ergodically a correctly trained RBM, because jumping from one cluster to another requires surpassing a very large free-energy barrier (note that the region between clusters has essentially zero probability by construction). Such a problem should, in practice, make the task of learning a good RBM, impossible in this kind of datasets. Indeed, one would need a prohibitive number of MC sweeps to compute the negative term of the gradient, and chains would never reach equilibrium even with standard methods such as PCD.

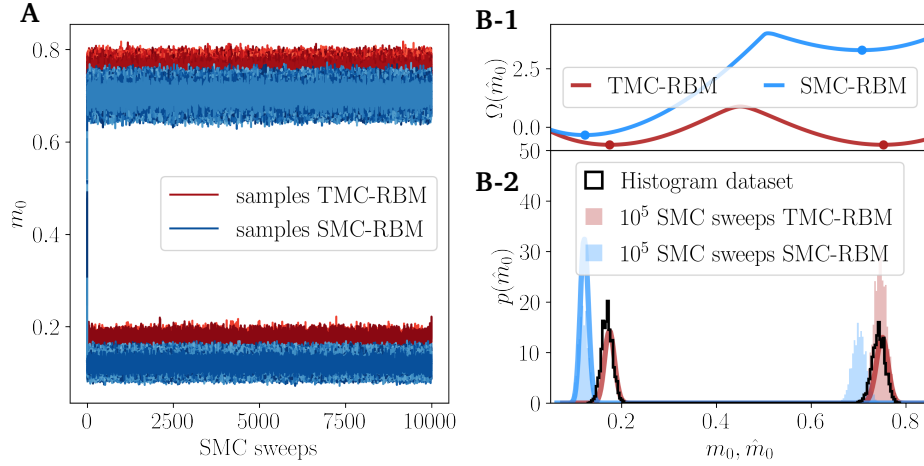


Figure 4: We compare RBMs trained with two different sampling procedures. We analyze models trained for 481 parameter updates, and a learning rates of 10^{-2} for the TMC-RBM and 10^{-4} for the SMC-RBM. The SMC-RBM is trained using PCD and 10 MC sweeps of Glauber dynamics (the standard procedure, SMC), and the TMC-RBM, is trained with PCD and 10 TMC1D sweeps fixing the projection m_0 . Once both machines are trained, we can sample their configuration space using SMC moves in **A**, or TMC moves in **B**. In **A**, we show the evolution of $m_0(t)$ for 1000 independent simulations initialized at random (in blue we show samplings of the SMC-RBM, in red, of the TMC-RBM). Fig. **A** shows that ergodicity is totally broken: Markov chains get trapped in the closest state found to with respect to its random initialization and not a single jump from one state to the other is ever observed. This means that thermalisation is not even close to being achieved and it is impossible to properly estimate the relative height of each of the two peaks from SMC simulations. In **B**, we sample both machines using the TMC algorithm instead to properly explore the equilibrium measure. TMC results are shown in thick solid lines. In **B-1**, we show the TMC effective potential $\Omega(\hat{m})$, displaying 2 relative minima for both models. We highlight the position of these minima with big dots. We can easily observe that they coincide with the mean projection of the two states we sampled in **A** with SMC. Yet, in the case of the SMC-RBM, the left-most minima is much lower, which is translated in a much higher TMC probability once $p(\hat{m})$ is computed in **B-2**. It is clear that non of the reconstructed equilibrium probabilities match the histograms obtained with the non-ergodic SMC sampling.

6.1.1 One-dimensional dataset

As anticipated, the 2 trained RBMs cannot be sampled ergodically using SMC moves as we illustrate in Fig. 4-A: simulations get trapped in one of the two metastable states from the very first MC sweeps and remain there at least until 10^5 MC sweeps. With this dataset, the learning of the SMC-RBM is very unstable, therefore we used different learning rate for the two RBMs: 10^{-2} for the TMC-RBM and a much slower one, 10^{-4} , for SMC-RBM. At this point, it is important to stress that one manages to generate points belonging to two different clusters only thanks to the random initialization of the Markov chains. In particular, we initialize each v_i as $\{0, 1\}$ with 50% of probability, which means that initial configurations have in average $m_0 \sim 0.5$, which depending on the profile of the potential Ω , tend trap the chains in the nearest free-energy minima, independently on its relative depth. Despite both RBMs generating data in two separate clusters, such clusters are not the same for the 2 machines. This is much clearer if we compare the distribution of the magnetizations m_0 of the generated samples after 10^5 SMC sweeps with each RBM, with those of the dataset, see Fig. 4-B2. Clearly the SMC-RBM generates samples in the wrong region (with wrong values of m_0) and this situation does not improve at all if we continue the learning for much longer. On the contrary, the samples generated with the TMC-RBM are at the right position. On Fig. 4-B2, we see only one (red) peak since the SMC is incapable of jumping from one cluster to the other, still the second peak would match the position of the dataset as can be checked on the panel A of the same figure.

As justified above, we can efficiently sample the phase-space of these two trained machines using the TMC sampling method (using simulations at fixed m_0). We show the results in plain lines in Fig. 4-B. In Fig. Fig. 4-B1, we show the Tethered effective potential Ω , as function of \hat{m}_0 , and in Fig. 4-B2, the reconstructed conditioned probability. As expected, the constrained free energy, Ω here, presents 2 minima at the two metastable states sampled before with SMC in Fig. 4-A, but their relative depth is significantly different for the SMC-RBM model. In the TMC-RBM case, the two minima have the same potential's value, meaning that they correspond to two states equally probable: the equilibrium distribution of the TMC-RBM match remarkably well with the dataset's distribution. Instead, in the case of the SMC-RBM, one minima is much higher than the other, and in fact, it is essentially suppressed in the equilibrium distribution $p(\hat{m}_0)$, see Fig. 4-B2. If we could wait long enough, all generated samples of the SMC-RBM would fall to the lower- m_0 minimum.

The conclusions of this simple experiment are rather worrying. First, when the clusters are well-separated in the learned RBM, the permanent chains of the classical training method remain trapped in one of the two clusters. The problem, here, is that it is impossible that the parallel chains are correctly balanced between the two minima of the potential. Still, since they can not escape from their local minimum, it gives the impression that the RBM is learning correctly the dataset while in reality the *true* equilibrium probability is not well-adjusted. This also means that the gradients cannot correct this problem. In fact, at longer training times, we observe that the SMC-RBM is not adjusting the location of the peaks correctly because of this effect.

We can illustrate this effect studying several intermediate models in the training of the SMC-RBM model, see Fig. 5-C where t_{age} refers to the number of parameters updates performed. In this figure, we compare: (i) the equilibrium constrained measure obtained with the TMC method, and the histogram of the m_0 of the samples either in (ii) the permanent chain, or (iii) obtained with a long SMC sampling. We also include, next to each distribution, the trajectory followed by several independent Markov chains during the SMC sampling. We can see that at, and below $t_{\text{age}} = 91$, each Markov chain jumps several times from one cluster to another in 5000 MC sweeps, and because of that the TMC $p(\hat{m})$ matches very well the distribution of the permanent and gen-

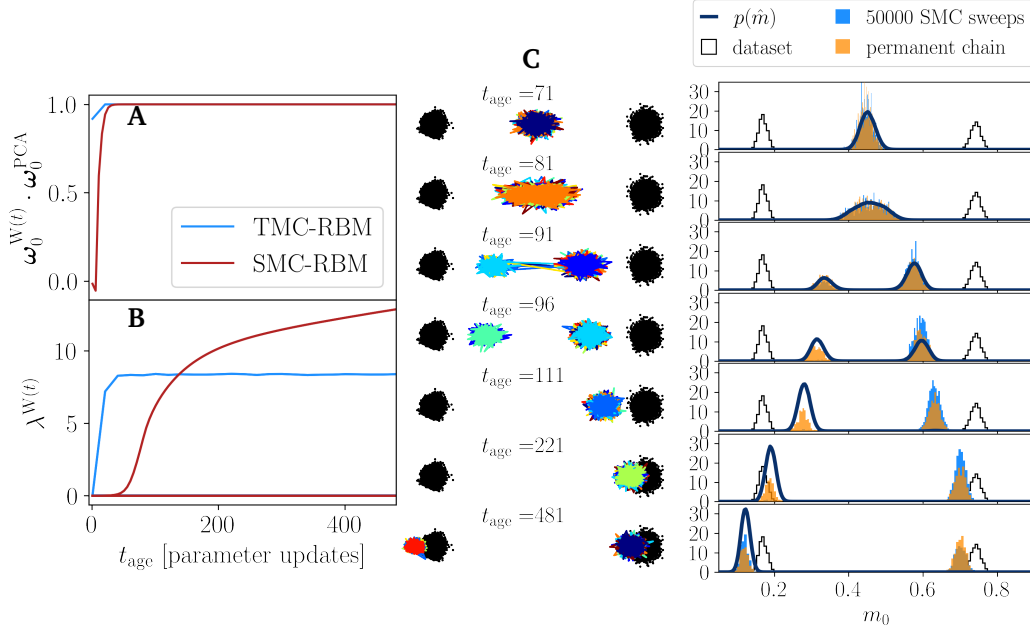


Figure 5: In **A** we show the projection of the first eigenvector of the RBM's weight matrix W , ω_0^W , on the direction of the first dataset's principal component ω_0^{PCA} , as a function of the number of parameter updates t_{age} , for a TMC-RBM and a SMC-RBM. In **B** we show the evolution of the eigenvalues of W for the two machines. Only the first eigenvalue is expressed, as only one direction is needed for this dataset. In **C** we investigate the SMC-RBM at 7 different stages of the training ($t_{\text{age}} = 71, 81, 91, 96, 111, 221, 481$ updates). In particular, we compare the equilibrium distribution of m_0 obtained with the TMC method, the histogram of the dataset, the histogram of the permanent chain during the learning, and the histogram of the samples generated with 50000 SMC sweeps. With the goal of illustrating the trapping phenomena, we show the trajectory of several Markov chains (in the $m_0 - m_1$ space) obtained during the SMC generation process.

erated samples, even when the distribution is bimodal. As the training progresses, for instance at $t_{\text{age}} = 96$ these jumps get rarer and rarer, which means that the permanent chains get trapped in each of the states with the proportion reached the last time the standard sampling was able of thermalising. Such proportion remains fixed for all the rest of the training, even if the equilibrium distribution of the model is actually unimodal. Neither the samples generated with standard MC moves are reliable .

Fig. 5-C let us illustrate another troublesome effect. Since the distribution of the permanent or generated chains differ strongly from that of the equilibrium, the negative term of the gradient is very badly computed and the learning trajectory is strongly affected by this. In fact, since the permanent chain is almost correctly located, the gradient is probably only adjusting little details of the parameters, while in reality, the equilibrium samples of the true model do not correspond to these samples and therefore the RBM end up very badly trained. Indeed the normal evolution of the training moves towards increasing the relative probability of the low m_0 state (the permanent chain contained an over-representation of high m_0 samples), which only contributes to suppress more and more the probability of the second state.

A sign of this training problem can be easily detected in this simple dataset by monitoring the eigenvalues of the weight matrix during the learning, λ_α . In this simple dataset, we observe that only the first eigenvalue λ_0 is turned on during the training. This λ_0 is associated to an eigenvector, ω_0^W , that in both kinds of machines, the TMC-RBM and the SMC-RBM, aligns perfectly with the first principal component of the dataset, ω_0^{PCA} in Fig. 5-A. Yet, the value of λ_0 does differ from one training to the other. Indeed, for the TMC-RBM, the learning stops at a given moment and the first eigenvalue remains constant from then and on. While in the SMC-RBM scheme, the λ_0 keeps growing as the gradient is not computed correctly. This is translated in a decrease of the effective temperature of the model (and a sharpening of the equilibrium peak that is appreciated in the compact trajectories of the $t_{\text{age}} = 481$ RBM in Fig. 5-C).

6.1.2 Two-dimensional dataset

We demonstrate again the feasibility of our approach for a case where the clusters span a two-dimensional subspace (see orange dots in Fig. 6). As in the 1D case, a SMC sampling fails to jump from one cluster to another one.

In this case, we rely on a 2D version of the TMC method. We need to constrain the magnetization along two principal directions because a single constraint is not able to split up the 3 clusters because they superimpose when projected on a single direction. A TMC-1D strategy would then suffer from convergence problems too (as the SMC). In this case, we show directly the results of the TMC approach, since it is clear from the previous example that the usual training algorithm cannot work. We show on Fig. 6 the TMC effective potential Ω extracted at various steps of the learning together with the projection of the dataset along the two chosen directions. On the last panel of Fig.6 (bottom-right) we plot the learning curves of the eigenvalues of the weight matrix. We see that, once the first two eigenvalues are learned, the machine stops evolving on linear timescale. Still, some more eigenvalues are increasing at large number of epoch indicating that we should probably lower the learning rate to stabilize the learning. We also show the evolution of the effective potential at different instants during the training process. We can appreciate how the potential adjust to fit the 3 different minima, and also how the final TMC reconstructed probability matches perfectly the distribution of the dataset in the $t_{\text{age}} = 1001$ figure. This shows how this strategy works perfectly on these difficult datasets.

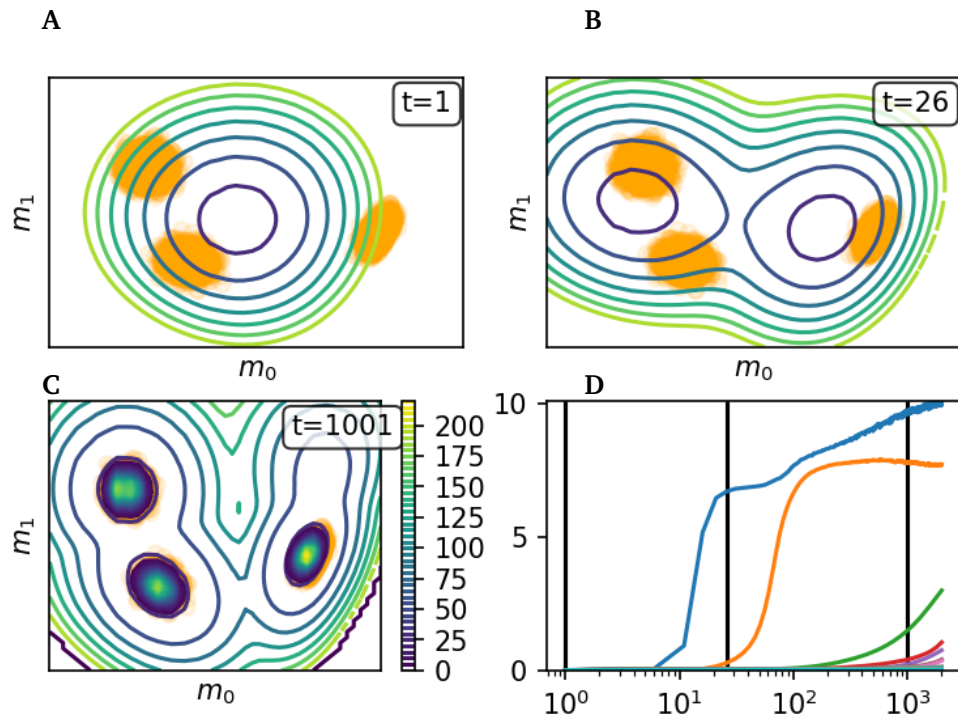


Figure 6: **A-C**: In orange dots, we show the m_0 and m_1 projections of the samples of a synthetic dataset of 3 clusters. In a contour map, we show the TMC effective potential Ω reconstructed at different moments of the training of a TMC-RBM (t_{age} refers to the number of updates). At $t_{\text{age}} = 1001$, we show also the TMC probability distribution (in a heatmap) that correctly reproduces the density of the three clusters. In **D**, we show the evolution of the W matrix eigenvalues as function of t_{age} .

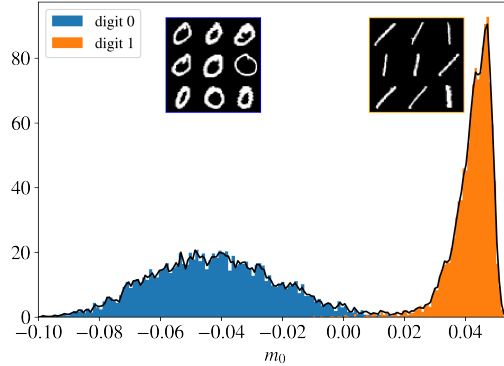


Figure 7: Histogram of the projection, m_0 , of all the samples of MNIST 0-1 dataset along its first principal component. We show in blue and orange, the histogram of the magnetizations of only the 0 and 1 digits. It is clear that m_0 separates efficiently both digits.

6.2 Real datasets

We now apply our TMC training method on real datasets. It is clear that big improvements are only expected in datasets that are clustered in some way. We therefore focus on two cases. First on the MNIST dataset reduced to the digits 0 and 1. It has been observed recently, that SMC samplings struggle to jump from one digit to another, making convergent generation samplings extremely long [34]. The second example is taken from the 1000 Human Genome Project [35], already studied in a generative context recently [14, 20]. In this last dataset, a strong clustered structure is observed when the data are projected along the first principal components of the dataset, $\{\omega_\alpha\}$.

6.2.1 MNIST 0-1 dataset

This dataset is built by taking only the digits 0 and 1 from the MNIST dataset [36]. We obtain slightly more than 10^5 images. At variance with the complete dataset, this reduced dataset splits into two well separated clusters when projected along ω_0 (the first principal direction of the dataset centered to zero), see Fig. 7.

In this example, we will again compare the performance of a TMC-RBM against a SMC-RBM. One critical moment in the training of this dataset, is when the first principal direction is learned. In this regime, the phase space of the RBM is made of two separated modes for which an SMC dynamics struggle to jump from one to another, while TMC should have no problem. Later in the training, as more and more directions are learned, we will see that the strong speed-up of TMC gets damped because the trained RBM seems to create alternative dynamic paths to jump from 0s to 1s that do not need to overcome this large barrier in m_0 . We can characterize these dynamical effects by computing the integrated autocorrelation times, τ_{int} [37], of $m_0(t)$ in the two different sampling dynamics.

In practice, what one observes is that, when only one direction has been learned, the relaxation time of the SMC dynamics is huge (not even measurable in “reasonable” times, and higher than 10^8), while the TMC relaxes in just some few steps. We estimate the SMC relaxation time in each RBM in Fig. 8–B. This divergence of times is related to the apparition of two very distant metastable states, see Fig. 8–A, just as we discussed in the contest of the artificial 1D dataset. Then, in a second phase of the learning, with the help of transverse directions learned by the

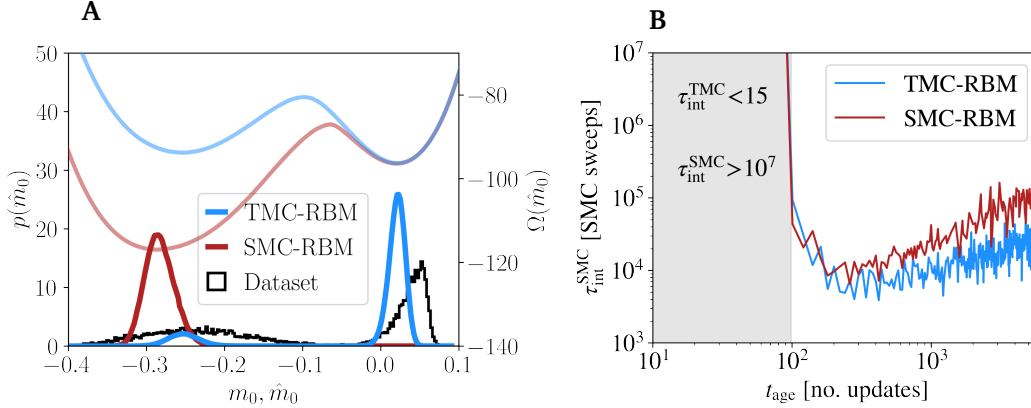


Figure 8: **A**: histogram of the dataset along the first direction ω_0 , together with the tethered potential $\Omega(\hat{m}_0)$ and the associated reconstructed TMC probability $p(\hat{m}_0)$ of both RBMs at the early stages of the learning (here, $t_{\text{age}} = 61$). We clearly observe the formation of two metastable states in both machines. In practice, we observe that Markov chains using SMC dynamics get trapped in one of these metastable states since initialization, and fail to visit the rest of the phase space. Just as described in the synthetic 1D dataset. **B**: We estimate the SMC integrated autocorrelation time $\tau_{\text{int}}^{\text{SMC}}$ of $m_0(t)$ as a function of the number of training updates used to train the two machines: TMC-RBM and SMC-RBM. The shaded area marks the region where $\tau_{\text{int}}^{\text{SMC}}$ overpasses 10^8 MC sweeps, while the $\tau_{\text{int}}^{\text{TMC}}$ (for the slower \hat{m} constraints) remains below 15 MC sweeps. When $t_{\text{age}} \gtrsim 10^2$, the SMC relaxation time drops to feasible values in both machines. Still, relaxational dynamics of the TMC-RBM is significantly faster than that of the SMC-RBM.

RBMs, the SMC relaxation time drops back to measurable values. Even if SMC thermalization times remain rather high, SMC sampling becomes competitive with respect to the TMC sampling in physical computation times, because TMC relaxation times grow fast as m_0 stops being able to break the metastabilities and because TMC sampling is much slower than SMC because the update of the visible variables cannot be parallelized. Yet, quite unexpectedly, we observe that TMC-RBMs have significantly faster relaxational SMC dynamics than SMC-RBMs, and that the factor between both grows with the number of parameter updates, see Fig. 8–B.

Finally, if we compare the two learned RBMs at $t_{\text{age}} = 1000$ parameter updates, we observe that the data generated by the TMC-RBM is quantitatively better than the SMC-RBM, and that the time it takes to jump from one cluster to another (from one digit to another) is much faster. Both phenomena are illustrated on Fig. 9.

6.2.2 Human genome dataset

We considered the population genetics’ dataset of Ref. [38]. This dataset corresponds to a subpart of the genome of a population of 5008 individuals, for which the alteration or not of a given gene is indicated by a $\{0, 1\}$ variable. A total of 805 genes are reported. For our study, the dataset was made of 4500 samples for the training set. This dataset has a very clustered nature, as can be appreciated in the dataset’s projection along the second and third principal directions shown in Fig. 10 where each dataset sample is represented as a black dot. One can also see that SMC dynamics get completely trapped in these different clusters in a well-trained machine, as we

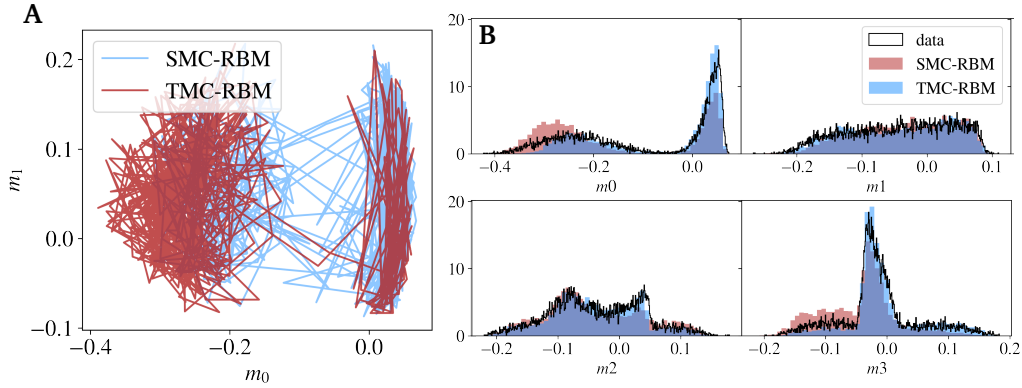


Figure 9: For an SMC-RBM and a TMC-RBM both trained for 1001 parameter updates with the same learning rate $\gamma = 0.01$ and the same $k = 10$, we show: **A**: For both machines, we show the scatter plot of the SMC dynamics projected along the first two directions: $m_1(t)$, $m_0(t)$, every 10^3 sweeps, for $5 \cdot 10^5$ SMC sweeps. One clearly appreciates that the sampling of the SMC-RBM is slower, given the reduced number of jumps (red curve) between the 0 and 1 states. **B**: The histogram of data generated by the two RBMs, in blue by the SMC-RBM and in orange the TMC-RBM, projected along the first four directions of the dataset’s principal directions. The black line correspond to the histogram of the dataset. Clearly, the SMC-RBM show much more anomaly than the TMC one.

illustrate with different color trajectories each corresponding to an independent sampling of the RBM.

We therefore constrain these directions for the training of the RBM using the TMC method. For this case, we will exhibit two clear advantages of this method. First, we show the feasibility of training the RBM on a real dataset using a set of two constrains. In this setting, the TMC method is not only useful to estimate better the negative term of the gradient, but it also gives the possibility to monitor how-well the equilibrium measure of the RBM is matching the data through the TMC effective potential. It is worth of mentioning that evaluating the quality of an RBM (that is, ensuring a proper adjustment of the density peaks with those of the dataset) with traditional SMC sampling methods is extremely hard, because jumps between the different metastable clusters are very rare and there are four of such clusters involved.

In fact, on Fig. 11 we show the TMC effective potential and the reconstructed distribution at various stages of the learning. It is interesting to see that it seems quite difficult to adjust correctly the 4 clusters to their correct weight. Thanks to the TMC method, we can easily track the position of the RBM’s clusters and diminish the learning rate to fine-tune the learning. On Fig. 11, we can see that after $t_{\text{age}} \approx 1200$, the TMC-RBM seems to be well-learned.

The second crucial improvement is that, only with the TMC method we can guarantee that all the clusters are visited regularly. Indeed, we already showed in Fig. 10 that we suffered strong break of ergodicity issues even after 10^5 SMC sweeps. This fact tells us that, on this dataset, each permanent chain of the PCD will remain trapped in certain regions of the phase space and will not be representative of the equilibrium measure of the RBM. As a consequence, the permanent chains will not estimate correctly the negative term of the gradient.

Finally, it is possible to try to train this dataset using the classical PCD - SMC algorithm. However, what we see is that the learning dynamics has a lot of trouble adjusting correctly the different

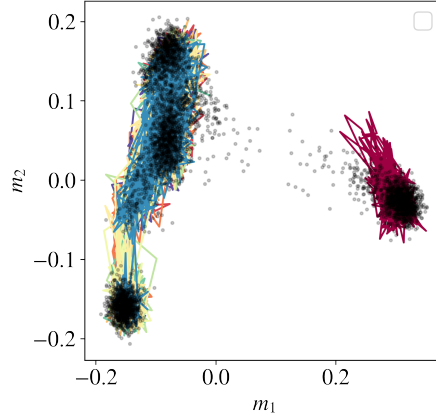


Figure 10: We show the training dataset projected along the second and the third principal directions (namely, m_1 and m_2) in black dots. The samples are grouped into separated clusters. In colorful solid lines, we show different SMC sampling trajectories $\{m_1(t), m_2(t)\}_t$ of 10^5 MC sweeps extracted from a TMC-RBM trained for $t_{\text{age}} = 1000$ updates, $\lambda = 0.01$ and $k = 10$. One can clearly appreciate that no jump is observed between the high and low m_1 sectors in this period.

minima, and that in addition, even if one can “cherry peak” the exact number of updates where the trained SMC-RBM has all the good dataset minima, such a process requires using the TMC method to track the presence of the good minima in the effective potential because SMC samplings are completely stuck. Even in that case, we observe that again TMC-RBMs relax faster than the equivalent SMC-RBM (for the same t_{age}). Yet, SMC dynamics are that slow for both kinds of machines, that computing $\tau_{\text{int}}^{\text{SMC}}$, as done in Fig. 8 for MNIST 0-1s, is beyond our numerical capacities. Still we can compare for both machines, the relaxation time in the TMC runs (which are much shorter). We obtain that $\tau_{\text{int}}^{\text{TMC}}[\text{SMC-RBM}] \sim 4 \cdot \tau_{\text{int}}^{\text{TMC}}[\text{TMC-RBM}]$, showing the the TMC-RBM is again faster than the PCD one.

7 Conclusion

We have demonstrated the feasibility, and the advantages, of using a biased Monte Carlo sampling strategy both for the training — that is, to estimate better the negative terms of the gradient to update the model’s parameters—, and for generating new samples in trained RBMs. Main improvements are observed for strongly clustered datasets, where classical local MCMC moves get stuck in one or several of these clusters and fail to sample ergodically (in reasonable times) the entire phase-space. At variance, we show that the Tethered Monte Carlo method is extremely efficient to sample the equilibrium measure of these kinds of models, as long as one can find good observables to uniquely identify each clusters. We show that the projection along the PCA first directions are good order parameters at the early stages of the training, as motivated from mean-field results [16, 32]. We show that this TMC strategy is crucial to learn correctly artificial low dimensional clustered datasets, datasets for which the standard learning approach combining parallel local MCMC updates with PCD completely fails to obtain reliable models for the data. For real datasets, we observe that, as learning progresses, more order parameters would be needed

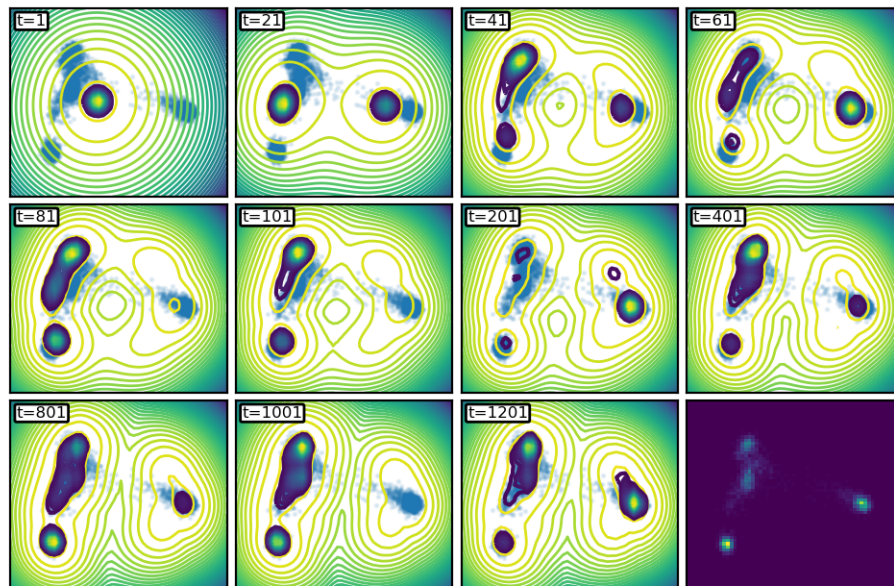


Figure 11: Evolution of the potential along the second and third principal direction during the learning of the TMC-RBM. We observe clear how the second direction is learned by the RBM, followed by third one. After a thousand parameter updates, the reconstructed probability distribution is covering the dataset.

to avoid the presence of metastabilities during the sampling, which means that the TMC strategy with just one or two constraints starts to suffer also ergodicity problems. Yet, we observe that even when TMC fails to thermalise easily, the trained models using a TMC sampling present significantly faster relaxational dynamics than those obtained with the standard approach.

In addition to all this, we observe that even for RBMs trained with standard sampling techniques, the TMC sampling approach is extremely useful for evaluating the quality of a given trained machine, given that it allows a direct computation of the probability distribution of the model projected along a set of chosen directions and thus giving the possibility to estimate how-well the model's distribution is matching the empirical one. The developed approach is thus a practical alternative to the most widely used Gibbs sampling algorithm when the intrinsic properties of the dataset drive the learning towards model with well-separated modes.

Despite the impressive performance of the TMC model in clustered datasets, it comes with a very two important drawbacks: first, it is much slower than the traditional alternate sampling in terms of computation time, because the global constraint introduces correlations between the visible (or hidden) variables thus breaking the conditional independence of the two layers. For this reason, alternative approaches involving only local constraints should be considered in the future to regain parallel performance.

Second, the dimensionality of the constraints. Since we need to integrate the potential accurately, we need to discretize the space in as many dimensions as the number of constraints, making the method cumbersome to use already with three constraints, and probably impossible for more.

Acknowledgments This work was supported by the Comunidad de Madrid and the Complutense University of Madrid (Spain) through the Atracción de Talento programs (Refs. 2019-T1/TIC-13298, for A.D. and 2019-T1/TIC-12776 for B.S.), and partially funded by PGC2018-094684-B-C21 funded by Ministerio de Economía y Competitividad, Agencia Estatal de Investigación and Fondo Europeo de Desarrollo Regional (FEDER) (Spain and European Union). N.B. wants to thanks the Theoretical Physics department at the University Complutense de Madrid for the welcoming and support during his stay.

References

- [1] P. Smolensky, *Information processing in dynamical systems: Foundations of harmony theory*, Tech. rep., Colorado Univ at Boulder Dept of Computer Science (1986).
- [2] D. H. Ackley, G. E. Hinton and T. J. Sejnowski, *A learning algorithm for boltzmann machines*, *Cognitive science* **9**(1), 147 (1985).
- [3] G. E. Hinton, *Training products of experts by minimizing contrastive divergence*, *Neural computation* **14**(8), 1771 (2002).
- [4] G. E. Hinton, S. Osindero and Y.-W. Teh, *A fast learning algorithm for deep belief nets*, *Neural computation* **18**(7), 1527 (2006).
- [5] G. E. Hinton and R. R. Salakhutdinov, *Reducing the dimensionality of data with neural networks*, *Science* **313**(5786), 504 (2006), doi:[10.1126/science.1127647](https://doi.org/10.1126/science.1127647), <https://www.science.org/doi/pdf/10.1126/science.1127647>.

- [6] I. Goodfellow, J. Pouget-Abadie, M. Mirza, B. Xu, D. Warde-Farley, S. Ozair, A. Courville and Y. Bengio, *Generative adversarial nets*, In Z. Ghahramani, M. Welling, C. Cortes, N. Lawrence and K. Q. Weinberger, eds., *Advances in Neural Information Processing Systems*, vol. 27. Curran Associates, Inc. (2014).
- [7] D. P. Kingma and M. Welling, *Auto-encoding variational bayes*, arXiv preprint arXiv:1312.6114 (2013).
- [8] J. Tubiana and R. Monasson, *Emergence of compositional representations in restricted boltzmann machines*, *Physical review letters* **118**(13), 138301 (2017).
- [9] K. Shimagaki and M. Weigt, *Selection of sequence motifs and generative hopfield-potts models for protein families*, *Physical Review E* **100**(3), 032128 (2019).
- [10] J. Tubiana, S. Cocco and R. Monasson, *Learning protein constitutive motifs from sequence data*, *Elife* **8**, e39397 (2019).
- [11] J. Tubiana, S. Cocco and R. Monasson, *Learning compositional representations of interacting systems with restricted boltzmann machines: Comparative study of lattice proteins*, *Neural computation* **31**(8), 1671 (2019).
- [12] T. L. van der Plas, J. Tubiana, G. Le Goc, G. Migault, M. Kunst, H. Baier, V. Bormuth, B. Englitz and G. Debrégeas, *Compositional restricted boltzmann machines unveil the brain-wide organization of neural assemblies*, *bioRxiv* (2021).
- [13] B. Bravi, J. Tubiana, S. Cocco, R. Monasson, T. Mora and A. M. Walczak, *Rbm-mhc: a semi-supervised machine-learning method for sample-specific prediction of antigen presentation by hla-i alleles*, *Cell systems* **12**(2), 195 (2021).
- [14] B. Yelmen, A. Decelle, L. Ongaro, D. Marnetto, C. Tallec, F. Montinaro, C. Furtlehner, L. Paganì and F. Jay, *Creating artificial human genomes using generative neural networks*, *PLoS genetics* **17**(2), e1009303 (2021).
- [15] H. Huang, *Statistical mechanics of unsupervised feature learning in a restricted boltzmann machine with binary synapses*, *Journal of Statistical Mechanics: Theory and Experiment* **2017**(5), 053302 (2017).
- [16] A. Decelle, G. Fissore and C. Furtlehner, *Thermodynamics of restricted boltzmann machines and related learning dynamics*, *Journal of Statistical Physics* **172**(6), 1576 (2018).
- [17] A. Barra, G. Genovese, P. Sollich and D. Tantari, *Phase diagram of restricted boltzmann machines and generalized hopfield networks with arbitrary priors*, *Phys. Rev. E* **97**, 022310 (2018), doi:[10.1103/PhysRevE.97.022310](https://doi.org/10.1103/PhysRevE.97.022310).
- [18] A. Decelle and C. Furtlehner, *Restricted boltzmann machine: Recent advances and mean-field theory*, *Chinese Physics B* **30**(4), 040202 (2021).
- [19] M. Harsh, J. Tubiana, S. Cocco and R. Monasson, *'place-cell' emergence and learning of invariant data with restricted boltzmann machines: breaking and dynamical restoration of continuous symmetries in the weight space*, *Journal of Physics A: Mathematical and Theoretical* **53**(17), 174002 (2020).

- [20] A. Decelle, C. Furtlehner and B. Seoane, *Equilibrium and non-equilibrium regimes in the learning of restricted boltzmann machines*, In A. Beygelzimer, Y. Dauphin, P. Liang and J. W. Vaughan, eds., *Advances in Neural Information Processing Systems* (2021).
- [21] D. Landau and K. Binder, *A guide to Monte Carlo simulations in statistical physics*, Cambridge university press (2021).
- [22] V. Nair and G. E. Hinton, *Rectified linear units improve restricted boltzmann machines*, In *Proceedings of the 27th International Conference on International Conference on Machine Learning*, ICML'10, p. 807–814. Omnipress, Madison, WI, USA, ISBN 9781605589077 (2010).
- [23] T. Tieleman, *Training restricted Boltzmann machines using approximations to the likelihood gradient*, In *Proceedings of the 25th international conference on Machine learning*, pp. 1064–1071 (2008).
- [24] A. Decelle and C. Furtlehner, *Exact training of restricted boltzmann machines on intrinsically low dimensional data*, *Physical Review Letters* **127**(15), 158303 (2021).
- [25] O. Krause, A. Fischer and C. Igel, *Algorithms for estimating the partition function of restricted boltzmann machines*, *Artificial Intelligence* **278**, 103195 (2020).
- [26] G. M. Torrie and J. P. Valleau, *Nonphysical sampling distributions in monte carlo free-energy estimation: Umbrella sampling*, *Journal of Computational Physics* **23**(2), 187 (1977).
- [27] R. Lustig, *Microcanonical monte carlo simulation of thermodynamic properties*, *The Journal of chemical physics* **109**(20), 8816 (1998).
- [28] V. Martin-Mayor, *Microcanonical approach to the simulation of first-order phase transitions*, *Physical review letters* **98**(13), 137207 (2007).
- [29] L. Fernandez, V. Martin-Mayor and D. Yllanes, *Tethered monte carlo: Computing the effective potential without critical slowing down*, *Nuclear physics B* **807**(3), 424 (2009).
- [30] L. Fernández, V. Martin-Mayor, B. Seoane and P. Verrocchio, *Equilibrium fluid-solid coexistence of hard spheres*, *Physical review letters* **108**(16), 165701 (2012).
- [31] V. Martin-Mayor, B. Seoane and D. Yllanes, *Tethered monte carlo: Managing rugged free-energy landscapes with a helmholtz-potential formalism*, *Journal of Statistical Physics* **144**(3), 554 (2011).
- [32] A. Decelle, G. Fissore and C. Furtlehner, *Spectral dynamics of learning in restricted boltzmann machines*, *EPL (Europhysics Letters)* **119**(6), 60001 (2017).
- [33] Y. Ichikawa and K. Hukushima, *Statistical-mechanical study of deep boltzmann machine given weight parameters after training by singular value decomposition*, *arXiv preprint arXiv:2205.01272* (2022).
- [34] C. Roussel, S. Cocco and R. Monasson, *Barriers and dynamical paths in alternating gibbs sampling of restricted boltzmann machines*, *Physical Review E* **104**(3), 034109 (2021).
- [35] . G. P Consortium et al., *A global reference for human genetic variation*, *Nature* **526**(7571), 68 (2015).

- [36] L. Deng, *The mnist database of handwritten digit images for machine learning research*, IEEE Signal Processing Magazine **29**(6), 141 (2012).
- [37] D. J. Amit and V. Martin-Mayor, *Field theory, the renormalization group, and critical phenomena: graphs to computers*, World Scientific Publishing Company (2005).
- [38] V. Colonna, Q. Ayub, Y. Chen, L. Pagani, P. Luisi, M. Pybus, E. Garrison, Y. Xue and C. Tyler-Smith, *Human genomic regions with exceptionally high levels of population differentiation identified from 911 whole-genome sequences*, Genome biology **15**(6), 1 (2014).